

## Research Article

# Wear Mechanism of Abrasive Gas Jet Erosion on a Rock and the Effect of Abrasive Hardness on It

Yong Liu <sup>1,2</sup>, Huidong Zhang <sup>1,2</sup>, Pathegama Gamage Ranjith,<sup>3</sup> Jianping Wei,<sup>1,2</sup> and Xiaotian Liu<sup>4</sup>

<sup>1</sup>State Key Laboratory Cultivation Base for Gas Geology and Gas Control, Henan Polytechnic University, Jiaozuo, 454000 Henan, China

<sup>2</sup>The Collaborative Innovation Center of Coal Safety Production of Henan Province, Jiaozuo, 454000 Henan, China

<sup>3</sup>Deep Earth Energy Laboratory, Department of Civil Engineering, Monash University, Building 60, Melbourne, Victoria 3800, Australia

<sup>4</sup>Safety Technology Training Institute, Henan Polytechnic University, Jiaozuo, 454000 Henan, China

Correspondence should be addressed to Yong Liu; [yoonliu@126.com](mailto:yoonliu@126.com)

Received 22 September 2018; Revised 24 November 2018; Accepted 17 December 2018; Published 7 February 2019

Guest Editor: Andrew Bunger

Copyright © 2019 Yong Liu et al. This is an open access article distributed under the Creative Commons Attribution License, which permits unrestricted use, distribution, and reproduction in any medium, provided the original work is properly cited.

The existing erosion models of abrasive gas jet tend to neglect the effects of the rebounding abrasive. To address this shortcoming, abrasive wear tests were conducted on limestone by using an abrasive gas jet containing different types of particles and with different standoff distances. The results indicate that erosion pits have the shape of an inverted cone and a hemispherical bottom. An annular platform above the hemispherical bottom connects the bottom with the side of the pit. The primary cause of the peculiar pit shape is the flow field geometry of the gas jet with its entrained particles. There is an annular region between the axis and boundary of the abrasive gas jet, and it contains no abrasive. Particles swirling around the axis form a hemispherical bottom. After rebounding, the abrasive with the highest velocity enlarges the diameters of both the hemispherical bottom and erosion pit and induces the formation of an annular platform. The surface features of different areas of the erosion pit are characterized using a scanning electron microscope (SEM). It can be concluded that the failure modes for different locations are different. The failure is caused by an impact stress wave of the incident abrasive at the bottom. Plastic deformation is the primary failure mode induced by rebounding particles at the sides of the hemispherical bottom. The plastic deformation induced by the incident abrasive and fatigue failure induced by the rebounding abrasive are the primary failure modes on the annular platform. Fatigue failure induced by rebounding particles is the primary mode at the sides of the erosion pits. The rock failure mechanism that occurs for particles with different hardness is the same, but the rock damaged by the hard abrasive has a rougher surface.

## 1. Introduction

Abrasive gas jets are widely used in surface treatment engineering such as in drilling and lacquer and rust removal from metals and ceramics [1–3]. In recent years, they have been introduced in unconventional oil and gas production [4–6]. In particular, the abrasive gas jet can assist in drilling coalbed methane, can avoid problems that often occur in water jet-assisted drilling such as borehole collapse, and have broad application prospects [7, 8]. An important theoretical basis for the application of an abrasive gas jet is the clarification

of its erosive wear mechanism on a rock. The existing abrasive-impact rock-breaking mechanisms are classified into two categories. In one type of mechanism, the focus is primarily on crack propagation on the surface and inside of the rock induced by the abrasive impacting the rock [9–12]. The concept of this rock failure mechanism is that when the abrasive impacts a rock, a stress concentration occurs on its contact surface, which leads to cracks on the rock surface. A part of the load propagates into the rock in the form of a stress wave and is superimposed on the crack surface of the rock, thus resulting in shear failure of the rock. The other

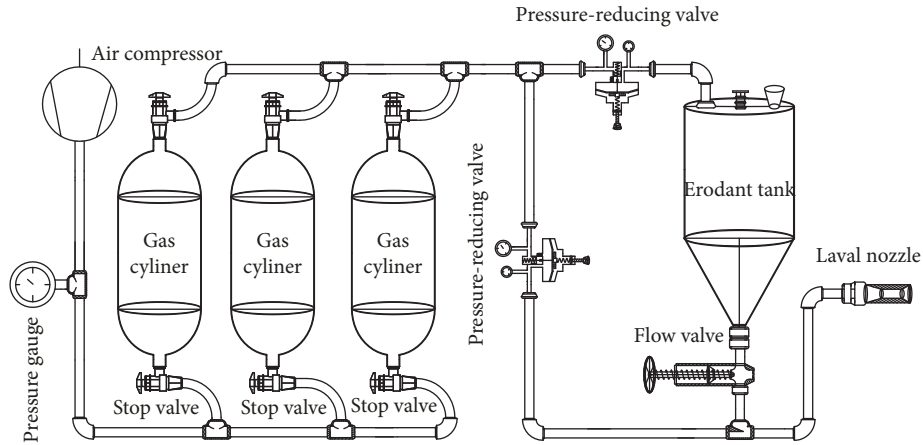


FIGURE 1: Schematic of connections in the high-pressure gas jet erosion system.

mechanism focuses on erosive wear. Analyzing the erosion morphology of a rock surface requires an understanding of the erosion wear mechanism of the abrasive. Intergranular brittle fracture and plastic flow are the two main mechanisms of material failure due to abrasive impact. Intergranular fracture is dominant during vertical impacts. However, both mechanisms play an equally important role in the case of a small-incident-angle impact [13–15]. Momber compared and analyzed the erosion wear characteristics of four types of rocks: porphyric rhyolite, Portuguese granite, Jurassic limestone, and argillaceous schist. He concluded that the surfaces of porphyric rhyolite and Portuguese granite showed lateral fractures. Lateral fractures, pileup, and lip formation were exhibited on the surfaces of Jurassic limestone and argillaceous schist. Plastic deformation was found to play a major role in schist erosion. Moreover, the rock-erosion wear formula considering plastic deformation and lateral cracking was established [16–20]. Regardless of the mechanism used for analyzing rock failure, it is necessary to first clarify and define the impact force of the abrasive. Numerous factors affect the impact force of an abrasive, such as the jet incidence pressure, erodent mass flow, and standoff distance. These three factors determine the velocity of an abrasive when it impacts a rock. However, in addition to the abrasive speed, the erosion wear of a rock is also related to the abrasive characteristics, such as its size, hardness, and shape. Therefore, it is difficult to describe the erosion wear mechanism of a rock using formulas. The existing erosion wear formulas only consider the primary erosion and neglect the effect of secondary erosion induced by rebounding particles. An abrasive impacts a rock surface and breaks into smaller abrasives, which rebound under the reacting force. These rebound abrasives can cut the rock effectively. Brown et al. believed that the effect of secondary erosion should not be neglected in high-angle erosion [21].

Deng et al. showed that there is a significant reduction in the specific erosion rate for high particle concentrations. This reduction was considered to be a result of the shielding effect induced by rebounding particles during particle impacts [22]. Macchini et al. also believed that the cause of shielding is the increased likelihood of interparticulate collisions, i.e., the high collision probability between incoming and rebounding

particles that reduces the frequency and the severity of particle impacts on the target surface [23]. The results of the study of Nguyen et al. also show that the change in erosion rates with the particle mass flow has been attributed to rebounding particles interfering with incident particles, resulting in a lower erosion rate [24]. In addition to the shielding effect, the collision frequency of particles when moving inside the system is another critical factor. It is believed that a strong interaction often happens at a higher impinging angle as well as at a higher particle mass flow or higher impinging velocity [25, 26]. A strong particle-particle interaction can cause a reduction in energy transfer to the surface, which, in turn, leads to a reduction in the erosion rate. Both the shielding effect and particle-particle interaction cause energy and velocity loss in the particle-surface collision [27]. Erosive gas jet-assisted drilling is mostly perpendicular erosion. Therefore, the effects of secondary erosion and rebound abrasive on the velocity of the incident abrasive and rock erosion cannot be ignored.

In this work, to clarify and define the erosion wear mechanism of a rock induced by abrasive gas jet, the erosion wear characteristics of the rock were analyzed by experiments along with the effect of the abrasive type. The failure characteristic of the rock surface eroded by abrasive gas jet was examined via a scanning electron microscope (SEM).

## 2. Erosion Experiment

**2.1. Experimental System.** A high-pressure experimental abrasive gas jet system is used for the experiment. It consists of a high-pressure air compressor, high-pressure gas cylinder, digital pressure gauge, pressure control valve, gate valve, abrasive tank, and operation box. The high-pressure air compressor has a maximum pressure of 40 MPa and maximum air intake of 2 m<sup>3</sup>/min, whereas the high-pressure gas cylinder has a maximum allowable pressure of 40 MPa. The system devices are connected as shown in Figure 1. The nozzle used is a Laval nozzle, whose structural parameters are displayed in Figure 2. Before the experiment, high-pressure gas is stored in the high-pressure gas cylinder and the outlet pressure is adjusted with the pressure-regulating valve. The inlet pressure ranges between 0 and 40 MPa, whereas

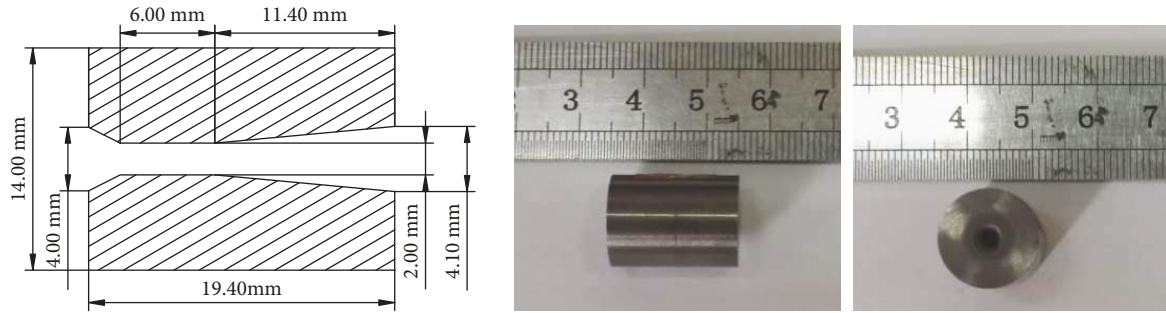


FIGURE 2: Nozzle structure parameters.

TABLE 1: Experimental parameters.

Pressure (MPa)	Abrasive	Abrasive mesh	Abrasive mass flow (g/s)	Standoff distance (mm)
15	Quartz sand/garnet/brown aluminum oxide/silicon carbide	80	16	100
15	Quartz sand/garnet/brown aluminum oxide/silicon carbide	80	16	120
15	Quartz sand/garnet/brown aluminum oxide/silicon carbide	80	16	150
15	Quartz sand/garnet/brown aluminum oxide/silicon carbide	80	16	200

the outlet pressure ranges between 0 and 25 MPa. The pressure-regulating valve, which has an adjustable outlet pressure accuracy of 0.1 MPa, can accurately control the jet pressure, thereby ensuring a constant jet pressure during the experiment to meet the experimental requirements. The high-pressure gate valve is installed below the abrasive tank to precisely control the mass flow rate of the abrasive. This gate is suitable for controlling the flow of the solid particles under high-pressure conditions. Before the experiment, the gate valve scale for the mass flows of the different abrasive is determined by calibration.

**2.2. Experimental Parameters.** Because numerous factors affect the erosion effect, e.g., the abrasive diameter, abrasive shape, and abrasive hardness [28–31], the experimental parameters of the abrasive and gas jet should be determined along with the engineering characteristics and technological status of erosive gas jet-assisted drilling. At present, widely used abrasives include quartz sand, garnet, brown corundum, and silicon carbide. From the perspective of hardness, brown corundum (Mohs hardness: 9) and silicon carbide (Mohs hardness: 9.5) have a better erosion effect than garnet (Mohs hardness: 8) and quartz sand (Mohs hardness: 7) but they have a greater negative effect on the service life of the nozzle [32–34]. An abrasive has an optimal particle size such that as the particle size increases, the erosion volume and depth first increase and then decrease [35, 36]. The maximum pressure of the existing high-pressure air compressor is up to 90 MPa, but its air inflow is low. Assisted drilling requires a high air inflow to remove the rock fragments well. An effective approach to achieve a high air inflow is decreasing the pressure of the air compressor. In the research results of Liu et al. and Wen et al. [7, 37, 38], the critical pressure for limestone breakage by abrasive gas jet was 15 MPa, which was set as the outlet pressure of the air compressor. The optimal abrasive size and mass flow were 80 meshes and 16 g/s,

respectively, when the gas pressure was 15 MPa. In addition to the jet and abrasive parameters, the standoff distance is an important factor affecting the erosion of the rock. The standoff distance essentially governs the impact velocity of the abrasive and thereby affects rock erosion. An abrasive is mainly accelerated in the nozzle and potential core of a free jet. The velocity of an abrasive increases continually in the potential core of the free jet section of a gas jet until a force, such as the drag force, virtual mass force, and pressure gradient force, cannot make the abrasive accelerate further. The standoff distance determines the acceleration length of the abrasive. At the optimal standoff distance, the abrasive can accelerate to the maximum velocity. Typically, if the standoff distance is optimal, the efficiency of rock breakage is the highest. However, this is impossible in engineering applications. The standoff distance depends on the length of the potential core; however, its length is not greater than the length of the potential core. In addition, the length of the potential core increases with the increase in the gas jet pressure. Therefore, it can be understood that the standoff distance indirectly depends on the gas pressure. The present research shows that the abrasive velocity reaches the maximum at a standoff distance of 100 mm when the jet pressure is 15 MPa and the mass flow of the abrasive is 16 g/s. However, it is difficult to maintain the standoff distance optimally and invariantly during operation. Consequently, the erosion wear characteristics of the rock need to be analyzed at different standoff distances. The experimental parameters are listed in Table 1.

**2.3. Experimental Phenomena.** Because many researchers have performed numerous interesting and relevant studies on the effect of the abrasive and gas jet parameters on the erosion wear depth and volume, these parameters are not analyzed in this study. This paper focuses on the failure models of a rock eroded by abrasive gas jets and the mechanisms of

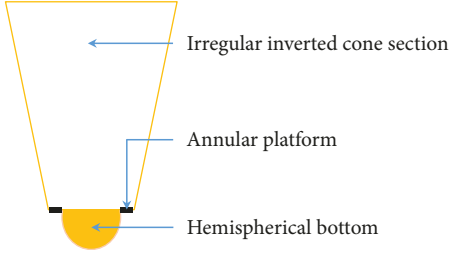


FIGURE 3: Schematic of the erosion pit.

the different failure models of the rock. The erosion characteristic of the rock sample reveals the occurrence of an interesting phenomenon in the erosion pits of the selected four types of abrasive at any standoff distance. Taking as an example a rock sample eroded by garnet abrasive to introduce this phenomenon shows that, generally, the erosion pit has an irregular conical shape. However, the shape of the bottom of the erosion pit is completely different from that obtained with a water jet or other jets. The bottom of the erosion pit is hemispherical. There is an annular platform above the hemispherical bottom that connects the bottom and side of the erosion pit, as shown in Figure 3. Figure 4 presents the shape of the erosion pit at different standoff distances.

The shape of the erosion pit is basically the same at different standoff distances. The upper part of the erosion pit has an inverted conical shape. An annular platform and a hemispherical bottom are located below the inverted conical shape. When the standoff distance is short, the diameter of the mouth of the erosion pit is short and the erosion pit is deep. With the increase in the standoff distance, the diameter of the mouth of the erosion pit increases and the depth decreases. When the standoff distance is 100 mm, the diameter of the mouth is 34.5 mm and the erosion depth is 34.34 mm. When the standoff distance is increased to 200 mm, the diameter of the mouth is 55.8 mm and the erosion depth is 25.4 mm. The width of the annular platform increases with the standoff distance. The width of the annular platform at the four standoff distances is 1.36 mm, 5.24 mm, 8.78 mm, and 10.5 mm, respectively. The depth of the hemispherical bottom is 6 mm, 7 mm, 8 mm, and 6.2 mm, respectively, and the erosion is the deepest at the standoff distance of 150 mm.

**2.4. Analysis of Experimental Phenomenon.** The distinct shape of the erosion pit of an abrasive gas jet is induced by the combination of the erosion of an incident abrasive and its rebound abrasive. If a rebound abrasive does not erode a rock surface, the shape of the erosion pit will be consistent with the sectional shape of the gas jet, as shown in Figure 5(a). After the erosion of a rock, the impact energy divides the abrasive into smaller pieces, which causes them to rebound with high velocity. A rebound abrasive continually erodes the wall of the erosion pit, increasing the pit's diameter, as shown in Figure 5(b). Therefore, the shape of the erosion pit depends on the gas jet shape and rebound abrasive. To clarify and define the effect of the gas jet and rebound abrasive on the shape of the erosion pit, the flow field structure of the gas jet and characteristics of the motion of the abrasive were numerically simulated in Fluent.

**2.4.1. Numerical Simulation Model.** The numerical simulation geometric model as designed based on the erosion parameters, such as the erosion pit parameters and nozzle parameter, and at a standoff distance of 100 mm is depicted in Figure 6. A structured grid is used for mesh division and the mesh number is 23160 based on the mesh sensitivity analysis. The inlet and outlet boundaries are the pressure inlet and outlet, respectively, and the wall surface is a nonslip wall. The inlet pressure is the same with the experiment pressure. The boundary condition of the erosion pit is a reflection wall. The discrete-phase reflection coefficient is used to represent the change in momentum after particle impact, which is calculated by a polynomial in terms of impacting angle. All the inlet temperatures are 300 K and outlet pressures are 0.1 MPa; the garnet abrasive is 3500 kg/m<sup>3</sup> and its diameter is 180 μm. The initial velocity of the abrasive depends on the gas jet velocity. The gas and solid phases are calculated based on a continuous-phase model and a discrete-phase model (DPM), respectively. After the gas phase becomes convergent and stable, the DPM starts to calculate the parameters of the abrasive, such as the velocity and spatial location.

In this study, for the gas phase, the RNG  $k-\varepsilon$  turbulence model can simulate, among other properties, the high-Reynolds number flow of the jets. The gas is assumed to be an ideal gas. The governing equations for the RNG  $k-\varepsilon$  turbulence model are [39]

$$\begin{aligned} \frac{\partial(\rho k)}{\partial t} + \frac{\partial(\rho k u_i)}{\partial x_i} &= \frac{\partial}{\partial x_j} \left( \alpha_k \mu_{\text{eff}} \frac{\partial k}{\partial x_j} \right) + G_k + G_b \\ &\quad - \rho \varepsilon - Y_M + S_k, \\ \frac{\partial(\rho \varepsilon)}{\partial t} + \frac{\partial(\rho \varepsilon u_i)}{\partial x_i} &= \frac{\partial}{\partial x_j} \left( \alpha_\varepsilon \mu_{\text{eff}} \frac{\partial \varepsilon}{\partial x_j} \right) + C_{1\varepsilon} \frac{\varepsilon}{k} (G_k + C_{3\varepsilon} G_b) \\ &\quad - C_{2\varepsilon} \rho \frac{\varepsilon^2}{k} - R_\varepsilon + S_\varepsilon, \end{aligned} \quad (1)$$

where

$$\begin{aligned} \mu_{\text{eff}} &= \mu + \mu_t, \\ \mu_t &= \rho C_\mu \frac{k^2}{\varepsilon}, \\ G_b &= \varphi g_i \frac{\mu_t}{Pr_t} \frac{\partial T}{\partial x_i}, \\ G_k &= -\rho u_j \mu_j \frac{\partial u_j}{\partial x_i}, \\ Y_M &= 2\rho \varepsilon \frac{k}{a^2}, \\ R_\varepsilon &= \frac{C_\mu \rho \eta^3 (1 - (\eta/\eta_0)) \varepsilon^2}{1 + \beta \eta^3} \frac{1}{k}, \\ \eta &= \frac{Sk}{\varepsilon}. \end{aligned} \quad (2)$$

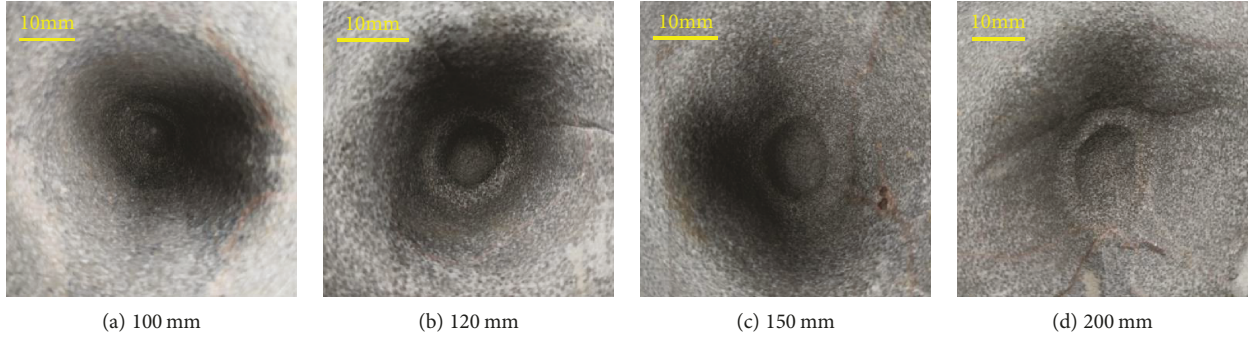


FIGURE 4: Features of the erosion pit at various standoff distances.

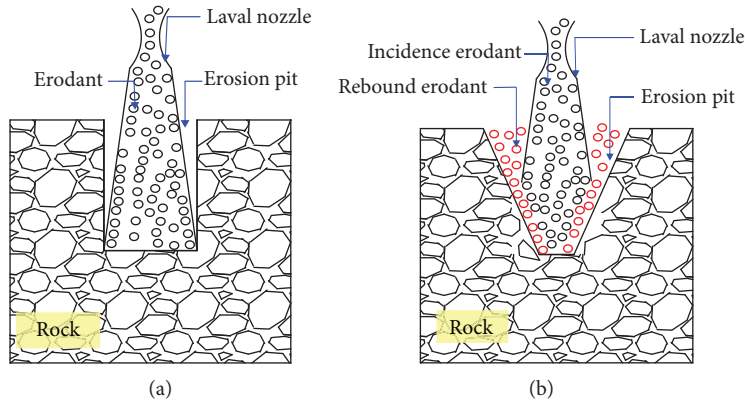


FIGURE 5: Schematic of the erosion pit feature: (a) is a hypothetical erosion pit feature without considering the rebound abrasive and (b) is a real erosion pit feature considering the reflection abrasive.

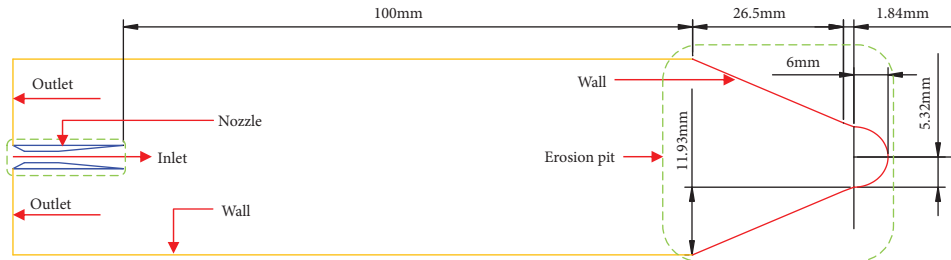


FIGURE 6: Numerical simulation geometric model.

$\rho$  is density;  $k$  is turbulent kinetic energy;  $\epsilon$  is the dissipation rate of  $k$ ;  $t$  is time;  $x_i$  are the Cartesian coordinates;  $u_i$  and  $u_j$  are velocity components along  $i$  and  $j$ , which are subscripts of tensors instead of tensors;  $\mu$  is gas viscosity;  $\mu_t$  is eddy viscosity;  $G_k$  is the generation term of the turbulent kinetic energy  $k$  resulting from the mean velocity gradient;  $G_b$  is the generation term of the turbulent kinetic energy owing to buoyancy;  $Y_M$  is the contribution of the fluctuating dilatation in compressible turbulence to the overall dissipation rate;  $\alpha_k$  and  $\alpha_\epsilon$  are the reciprocals of the effective Prandtl numbers for turbulent kinetic energy and dissipation rate, respectively;  $Pr_t$  is the turbulence Prandtl number;  $C_{1\epsilon}$ ,  $C_{2\epsilon}$ , and  $C_{3\epsilon}$  are empirical constants;  $g_i$  is the component of gravitational acceleration in the  $i$  direction;  $\varphi$  is the thermal expansion coefficient; and  $a$  is the acoustic velocity,  $S$  is the modulus

of the mean rate-of-strain tensor,  $C_\mu$  and  $\eta_0$  are both constants, and  $S_k$  and  $S_\epsilon$  are user-defined source terms.

The DPM is introduced in the solid-fluid flow to simplify the simulation of the motion in the particle phase. The DPM can be used to calculate the trajectories of a portion of the particles in the discrete phase; nevertheless, a simulation of the particle motion with a universal application value can be performed. The motion of the coal particles is defined by the Lagrangian multiphase flow model. The pressure and drag forces on the particles are calculated in a Lagrangian framework. The velocity distribution of the particles can be evaluated by the force balance on the particle. The governing equation is as follows [40–42]:

$$m_p \frac{d\vec{u}_p}{dt} = \vec{F}_D + \vec{F}_G + \vec{F}_B + \vec{F}_L + \vec{F}_{VM} + \vec{F}_B + \vec{F}_P, \quad (3)$$

where  $m_p$  is the particle mass,  $\vec{u}_p$  is particle velocity,  $\vec{F}_D$  is drag force vector,  $\vec{F}_G$  is gravity force vector,  $\vec{F}_B$  is Magnus buoyancy force vector,  $\vec{F}_L$  is lift force vector,  $\vec{F}_{VM}$  is virtual mass force vector, and  $\vec{F}_P$  is pressure gradient force vector.

$$F_D = \frac{3\mu_m C_D \text{Re}_p}{4d_p^2 \rho_p} (\vec{u}_f - \vec{u}_p), \quad (4)$$

where  $u_f$  is the velocity of the fluid,  $\rho_p$  is the density of the particle,  $d_p$  is the diameter of the particle,  $\mu_m$  is dynamic viscosity,  $C_D$  is the drag coefficient, and  $\text{Re}_p$  is the relative Reynolds number.

$$\vec{F}_G + \vec{F}_B = \frac{(\rho_p - \rho)}{\rho_p} g \cdot \vec{e}, \quad (5)$$

where  $\vec{e}$  is a unit vector.

$$\vec{F}_{VM} = C_{VM} \frac{\rho}{\rho_p} \frac{d}{dt} (\vec{u}_f - \vec{u}_p), \quad (6)$$

where  $C_{VM}$  is the virtual mass coefficient.

$$\vec{F}_L = C_L \frac{\rho}{\rho_p} (\vec{u}_f - \vec{u}_p) \times \nabla \times \vec{u}, \quad (7)$$

where  $C_L$  is the lift coefficient.

$$\vec{F}_B = \frac{3}{2} d_p^2 \sqrt{\pi \rho \mu_m} \int_{t_0}^t \frac{(d/d\tau)(\vec{u}_f - \vec{u}_p)}{\sqrt{t - \tau}} d\tau, \quad (8)$$

where  $\tau$  is the time variable.

$$\vec{F}_P = -V_p \nabla P, \quad (9)$$

where  $V_p$  is the particle volume.

The solid-phase angular momentum equation is

$$I \frac{d\vec{\omega}}{dt} = \vec{T}, \quad (10)$$

where  $I$  is the moment of inertia,  $\vec{\omega}$  is particle angular velocity, and  $\vec{T}$  is torque.

**2.4.2. Analysis of Numerical Simulation Results.** When the gas flows through the nozzle, the static pressure decreases gradually, which leads to the increasing of gas velocity. Because the gas velocity is less than the velocity of sound at the entrance of the nozzle, the gas accelerates in the convergent section of the nozzle. When the gas flows into the throat section, the gas

accelerates in the first 1 mm. Then the acceleration is inapparent in the middle section of the throat, because the static pressure is barely changed and velocity is approximately equal to sound velocity, as shown in Figures 7(a) and 7(c). When a gas jet is ejected from a nozzle, the jet pressure decreases and the velocity increases. The gas jet compresses the surrounding air to form an expansion wave. When the static pressure of the gas jet is equal to the boundary pressure, the expansion wave reflects and superposes to form a compression wave. The expansion and compression waves alternately develop forward to form a free jet section, as shown in Figures 7(b) and 7(d). The pressure and density of the expansion and compression waves are not uniformly distributed, which induces the uneven distribution of the abrasive in the gas jet. The abrasive velocity at the axis of the jet reaches the maximum value of 290 m/s, which is higher than the velocity at the boundary of the gas jet. However, abrasives with high velocity are obviously fewer at the boundary. The primary interesting feature of the flow field structure of the abrasive gas jets is the presence of an annular region without an abrasive between the axis and boundary, as shown in Figure 8(a). When the abrasive gas jets reach the rock surface, the jet radius  $R_j$  is smaller than the radius  $R_p$  of the mouth of the erosion pit. Therefore, this verifies that the rebound abrasive mainly results in an increase in the diameter of the erosion pit. As presented in Figure 8(b), the rebound abrasive collides with the incident abrasive after impacting the rock, which reduces the velocity of the incident abrasive. In addition, with the increase in the number of rebound abrasives, the velocity of the incident abrasive continuously decreases, as shown in Figure 8(c).

The rebound of an abrasive significantly affects the shape of the erosion pit and distribution of the abrasive velocity. Therefore, the effect of the rebound abrasive cannot be ignored in the analysis of the erosion pit shape. When an abrasive exactly reaches the rock surface, in the absence of the effect of the rebound abrasive, the abrasive velocity at the axis of the jet is high. The abrasive applies an impact force on the rock surface, which is transmitted into the rock in the form of stress waves, including longitudinal, transverse, and Rayleigh waves. The longitudinal and transverse waves propagate in the rock, whereas the Rayleigh wave propagates on the rock surface. The longitudinal wave propagates within the solid in a compression-tension manner, which will generate a radial tensile stress when the wave front rapidly expands forward [11]. However, the abrasive motion in the transverse wave is perpendicular to the propagation direction, which can generate a shear stress and circumferential tensile stress in the rock [43]. The Rayleigh surface wave, with vertical and horizontal components, will accordingly induce tensile and shear stresses. The tensile and shear stresses generated by the abrasive impact may account for the initiation and extension of the cracks in the rock. Moreover, the interference and reflection of the different waves will result in the reinforcement of the stress wave, which is conducive to the generation of cracks [44].

When more abrasives simultaneously impact the rock surface, the cracks formed by the impact of each abrasive intersect with each other, which leads to rock damage.

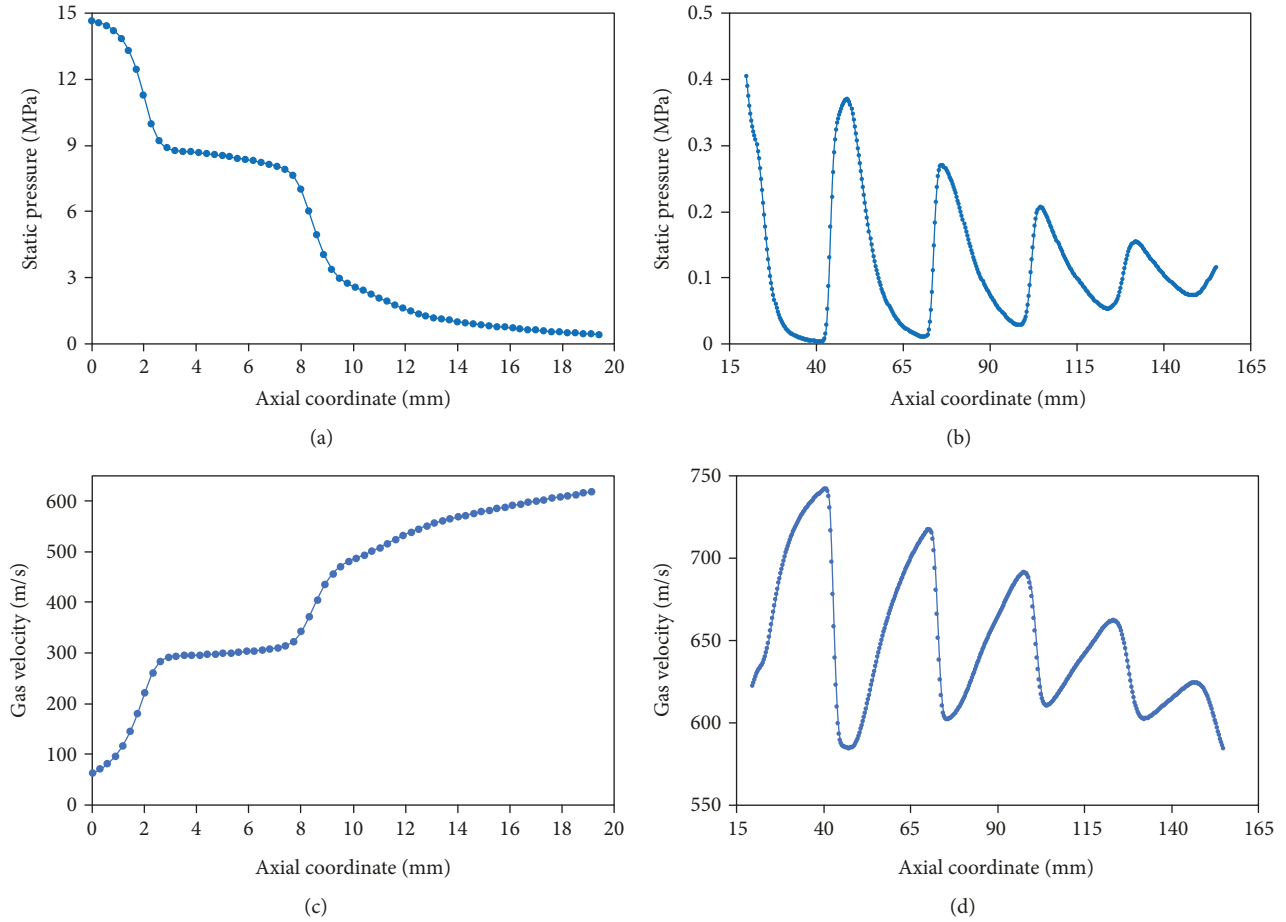


FIGURE 7: The static pressure and velocity of the gas jet.

Because the stress wave propagates in the rock in the form of spherical waves [45], the initial shape of the erosion pit rock surface is sphere like. After impacting the rock, the abrasive begins to rebound because of the reactive force. The abrasive is vertically incident, and the rebound angle is large. However, under the obstruction of an incident abrasive, the rebound abrasive moves along the bottom surface of the erosion pit (Figure 9(a)), secondarily erodes the surface of the erosion pit, and increases the diameter of the hemispherical bottom. With the increase in the number of rebound abrasives and depth of the erosion pit, the rebound abrasive not only erodes the side of the hemispherical bottom but also moves along the side of the erosion pit, eroding it and increasing its diameter (Figure 9(b)). Because of the presence of the annular region in the abrasive gas jets without an abrasive, the rebound abrasive tends to move toward the annular region (Figure 9(c)). The rebound abrasive in the annular region erodes the side of the erosion pit and promotes the formation of the annular platform, which connects the erosion pits between the bottom and side. Moreover, the volume and diameter of the erosion pit continuously increase. With the increase in the rebound abrasive and erosion time, the former affects the velocity of the incident abrasive more significantly. Only a small part of the incident abrasive can maintain a high velocity, continuously form cracks in the

rock, and increase the diameter of the hemispherical bottom. The rebound abrasive not only affects the velocity of the incident abrasive but also leads to the randomized direction of the abrasive velocity at the bottom of the erosion pit. Only a part of the high-velocity abrasive can continue to be perpendicular to the direction of incidence and erode the erosion pit. This implies that although the rebound abrasive plays an important role in increasing the volume and diameter of the erosion pit, they have an adverse effect on the increase in the depth of the erosion pit.

The incident and rebound abrasives jointly affect rock erosion. The incident abrasive of the jet axis can form a spherical stress wave, which leads to the formation of a hemispherical bottom at the base of the erosion pit. The rebound abrasive increases the diameter of the hemispherical bottom and form an annular platform by combining the effect of the annular region of the abrasive gas jets. The annular platform connects the hemispherical bottom and side of the erosion pit; however, there is a clear boundary. The rebound abrasive that moves along the wall of the erosion pit increases its diameter.

The flow field structure of the abrasive gas jets, and the characteristics of the abrasive movement are the main reasons for the characteristics of the erosion pit. In the erosion process, some regions are eroded by the combination of the

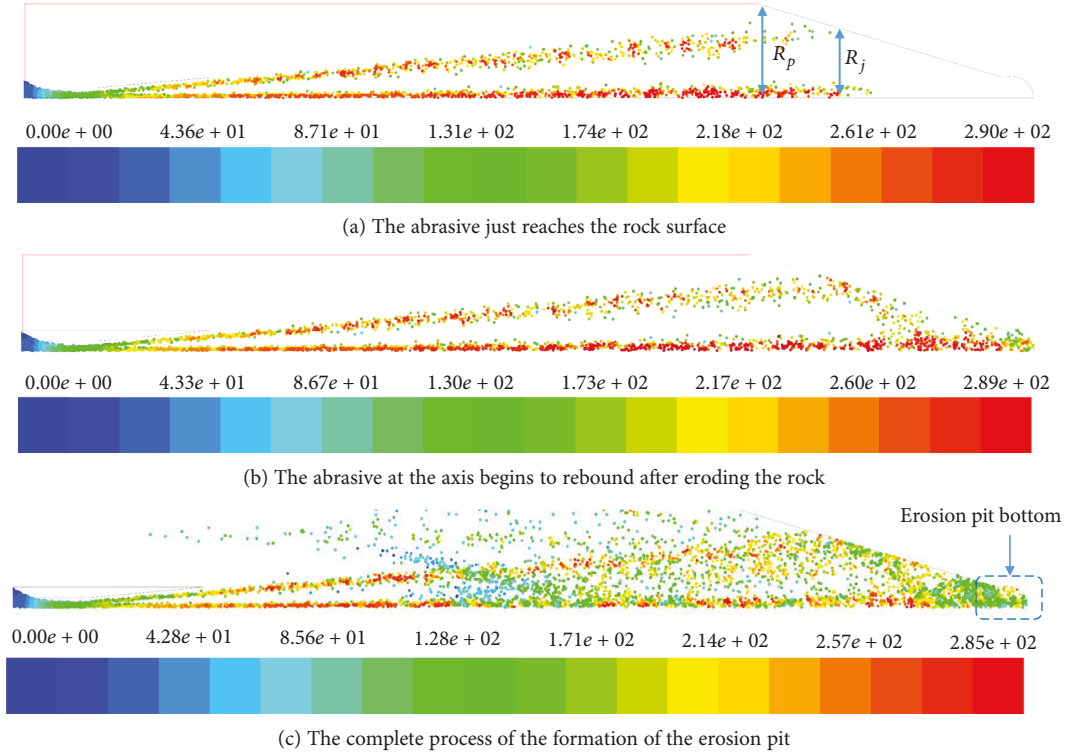


FIGURE 8: Flow field structure and velocity distribution of the abrasive gas jets during erosion of the rock.

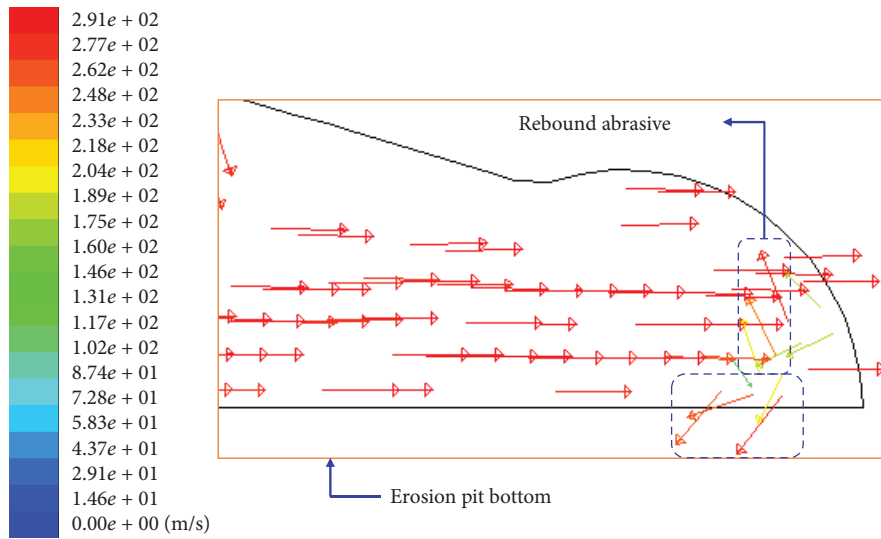
incident and rebound abrasives, whereas other regions are eroded separately by an incident abrasive or rebound abrasive. There is no strict distinction between an incident abrasive and a rebound abrasive for abrasive erosion, and some studies have even neglected the role of the rebound abrasive. From the above analysis, it can be seen that rebound abrasives play an important role in rock erosion. Therefore, it is necessary to analyze the erosion mechanism of the rebound abrasive.

### 3. Rock Erosion Mechanism

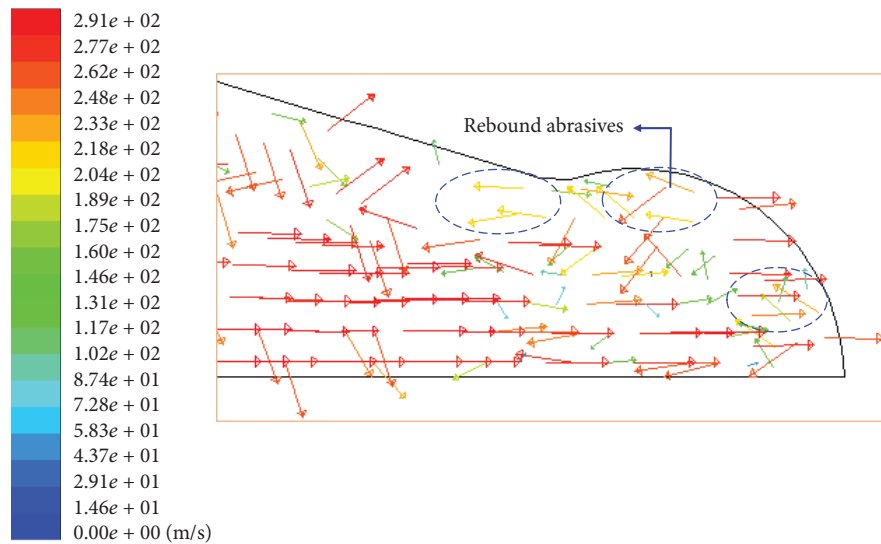
**3.1. Erosion Mechanism.** To clarify and define the erosion mechanism of the abrasive gas jets, the erosive rock was scanned by a SEM manufactured by the Field Electron and Ion Company. The model is FEI quanta 250FEGG, with a resolution of 2.5 nm and voltage of 10 kV. Considering as an example the rock eroded by a garnet abrasive, the base and side of the hemispherical bottom, annular platform, and erosion pit side were scanned based on the different erosion regions of the incident and rebound abrasives, respectively (Figure 10).

The result of the SEM of the limestone eroded by garnet is displayed in Figure 10. As shown in Figures 11(a)–11(d), the failure characteristics of the rocks are different in various parts of the erosion pit. Fractures (denoted as “F”) and lip formation (denoted as “P”) occur on the surface at the base of the hemispherical bottom, as shown in Figure 11(a) and the part marked with “ $\Delta$ ” in Figure 11(b). The fractures, which are distributed irregularly, partly connect to a larger fracture that transmits through the rock surface. The area

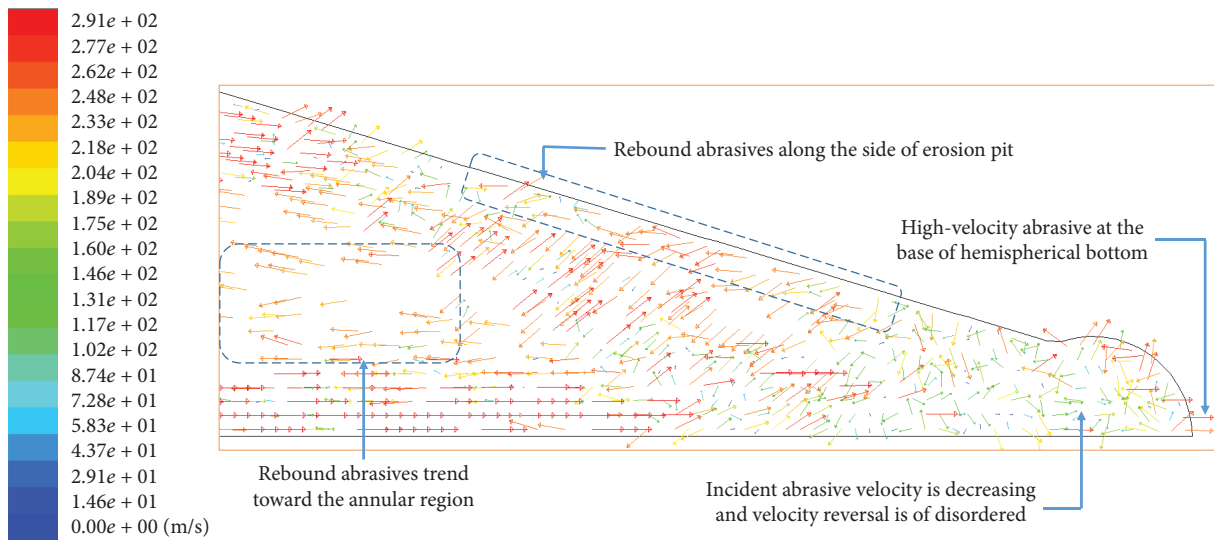
of the rock surface without a fracture appears clearly as a discontinuous lip formation. Thus, the area without the fracture or lip formation of the rock surface is the original surface that is not eroded by the abrasive. In addition, there is no residual abrasive at the base of the hemispherical bottom. The results of the SEM and numerical simulation of the abrasive motion characteristics can reveal the mechanism of rock erosion by abrasive gas jets. It is known from the results of the previous section that only a part of the high-velocity abrasive impacts the rock surface because of the shield effect of the rebound abrasive. The impact force of a high-speed abrasive can cause a brittle rupture of the rock, inducing a fracture on the surface and inside the rock [46]. The fractures formed by the adjacent abrasive connect to each other to form through the fracture, which strips one part of the rock mass from the surface and forms rock fragments. The impact force of a low-velocity abrasive is too small to cause a brittle fracture but is sufficiently large to press the abrasive into the rock surface and induce plastic flow of the rock. This leads to the formation of pits and flanges, namely, lip formation. When the second abrasive presses into the pit and surrounding flanges, the plastic flow will occur again. Such repeated plastic deformation and work hardening finally cause the rock to gradually harden and drop off brittly [20]. The number of fractures is obviously larger than that of lip formations, and there is no residual abrasive at the base. It can be identified that the rock mass is peeled off after the fractures are being transmitted through the rock. Therefore, the stress wave formed by the impact force is the main reason for the rock failure at the base of the hemispherical bottom.



(a) Abrasive begins to rebound at the base of the hemispherical bottom



(b) Rebound abrasives obstruct the incident abrasive and erode the side of the erosion pit



(c) Rebound abrasives tend to move toward the annular area

FIGURE 9: Abrasive distribution and motion direction of the abrasive during rock erosion by the abrasive gas jets.

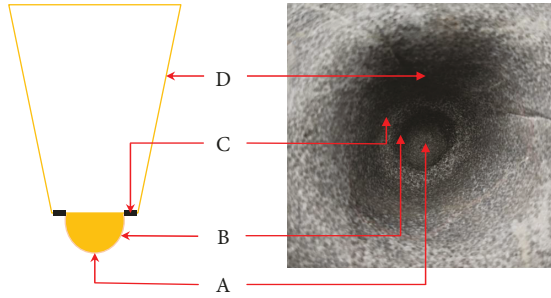


FIGURE 10: Position of scanning electron microscope. (A) Base of the hemispherical bottom. (B) The side of the hemispherical bottom. (C) Annular platform of the erosion pit. (D) The side of the erosion pit.

The failure characteristics of the side of the hemispherical bottom are obviously different from those at the base (in Figure 11(b), the triangle mark section is the base of the hemispherical bottom). From the comparison, it can be found that the failure of the side of the hemispherical bottom is mainly characterized by lip formation and there is a residual abrasive (marked with “O” in Figure 11(b)). The results of the numerical simulation exhibit that the side of the hemispherical bottom is mainly eroded by the rebound abrasive. The diameter of the rebound abrasive decreases because of the breakage of the incident abrasive after impact with the rock. The velocity of the rebound abrasive decreases because of the blockage of the incident abrasive. Therefore, the impact force of the abrasive applied on the side of the hemispherical bottom cannot lead to brittle rupture of the rock; it instead causes plastic deformation. The angle of embedding of the residual abrasive shows that the impact angle of the abrasive is large, similar to the result of Figures 9(b) and 9(c). Therefore, the rebound abrasive only leads to lip formation on the side of the hemispherical bottom.

Figure 11(c) is the SEM image of the annular platform of the erosion pit; the area marked with “□” is the boundary between the annular platform (upper section) and the side of the hemispherical bottom (lower section). The failure characteristics of the annular platform are similar to those of the side of the hemispherical bottom. Lip formation is the main failure characteristic of the annular platform, i.e., the rock of the annular platform fails primarily with the characteristic of plastic deformation. In addition, there are lateral cracking (denoted as “L”) and residual abrasives but the residual abrasives are embedded at a shallow depth. According to the results of the numerical simulation, the rebound abrasive purely and simply erodes the annular platform. The failure mechanism of the rock is different owing to the different erosion angles of the rebound abrasive. When the erosion angle of the abrasive is large, the abrasive can produce lip formation on the rock surface. When the erosion angle of the abrasive is small (almost parallel to the rock surface), the abrasive will roll easily on the rock surface and will not effectively erode the wear rock. However, some abrasive can erode the rock and form flake-like lateral cracking when their angle is between those abrasives that can cause lip formation and rolling. When the abrasive moves to the annular

platform, the velocity is lower than that at the hemispherical bottom. The normal stress of the impact force of the abrasive is lower than the yield limit of the rock, which cannot cause plastic deformation of the rock. However, the impact frequency of the abrasive is higher, which is equivalent to applying cyclic stress on the rock. If a rock only undergoes elastic deformation, there would be no damage but the rock surface will be hardened [47]. When the cyclic stress is further applied, a hardened slip plastic deformation layer and crack appear on the rock surface and the crack is parallel to the movement direction of the abrasive. This is consistent with the delamination theory proposed by Suh et al. [48].

The velocity of the rebound abrasive continuously decreases with its upward motion. Instead of plastic deformation, flake-like lateral cracks are formed on the rock surface (as shown in Figure 11(d)). The main failure form of the side of the erosion pit is fatigue damage caused by the cyclic stress of the rebound abrasive, which is consistent with the research results of Momber [19, 20] and Verhoef [49]. However, they failed to specify whether the erosion was of the incident or rebound abrasive.

From the above analysis, it can be concluded that the incident and rebound abrasives jointly erode the rock. However, they erode different parts separately and their erosion mechanisms are also different. At the base of the hemispherical bottom, the impact stress wave of the incident abrasive causes the expansion and connection of the fracture on the rock surface and inside the rock, which leads to rock failure. At the side of the hemispherical bottom, plastic deformation is the main failure characteristic and is induced by the rebound abrasive with a large impact angle. At the annular platform, in addition to the rock failure caused by the plastic deformation induced by the incident abrasive erosion, there is also fatigue failure caused by the rebound abrasive with a low impact angle. At the side of the erosion pit, fatigue failure is the main characteristic, which is induced by the rebound abrasive.

### 3.2. Influence of Abrasive Hardness on Erosion Failure.

The other eroded rock samples were scanned by the SEM with the same method, and the scanning results are shown in Figure 12. Figures 12(a) and 12(b) are the quartz sand-eroded images of the side and bottom, respectively, of the erosion pit. Figures 12(c) and 12(d) are brown aluminum oxide-eroded images of the side and bottom, respectively, of the erosion pit. Figures 12(e) and 12(f) are the silicon carbide-eroded images of the side and bottom, respectively, of the erosion pit. By comparing and analyzing the erosion images of the side and bottom of the erosion pit, it can be concluded that lateral cracking is the main failure of the side of the type of erosion pits but the roughness of the surface is different. The surfaces eroded by brown corundum and silicon carbide are obviously rougher than those eroded by quartz sand. The roughness of the rock surface eroded by silicon carbide is greater than that by brown corundum. There is an intergranular fracture due to fatigue stress on the sides of the erosion pits eroded by the brown corundum and silicon carbide, and the fracture surface is smooth. This indicates that the erosion wear mechanism of the side of

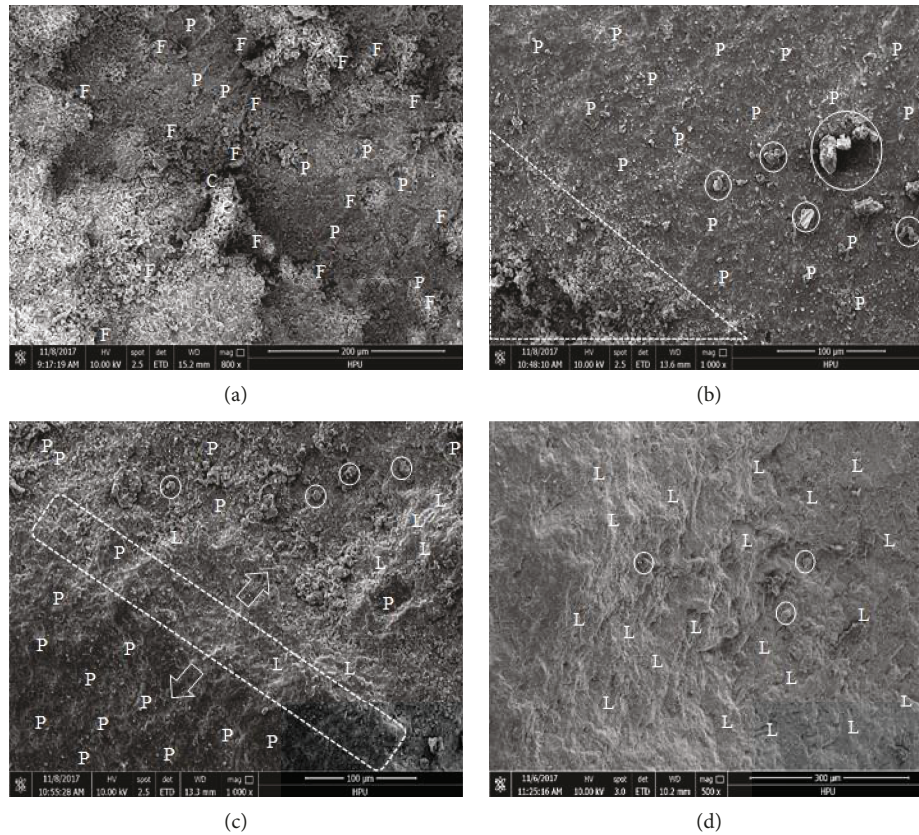


FIGURE 11: SEM images of the eroded limestone section.

the erosion pit is not related to the abrasive hardness but is only relevant to the direction of the force of the abrasive. The wear mechanism of the side of the erosion pit is the fatigue failure caused by the shear force of the rebound abrasive with a low incidence angle. The abrasive with a higher hardness is more difficult to destroy, and the energy dissipation on the new surface of the abrasive is small. Therefore, the energy conversion rate of a harder abrasive is higher. Thus, when the energy of the incident abrasive is the same, the force of the harder abrasive on the rock is greater, resulting in a larger range of elastic deformation of the rock. When fatigue failure occurs, the diameter of the peeling rock is larger, leaving a rough erosion surface.

The rock failure at the base of the hemispherical bottom of the three erosion pits is the same as that of the erosion pit eroded by garnet, and the fracture is the main failure characteristic. In addition, lip formation occurs due to the plastic deformation on the rock surface. As is the difference in the side of the erosion pit, the rock surfaces of the base of the hemispherical bottom eroded by brown corundum and silicon carbide have greater roughness. The incident and rebound abrasives jointly erode the rock of the base of the hemispherical bottom. In addition, the impact velocity and impact angle are both large, which leads to the formation of a fracture on the surface and inside the rock. The hard abrasive has a higher rebound velocity. The influence area and fragment size of the peeling rock are larger. Therefore, the rock surface is rougher.

From the comparative analysis, it can be concluded that the abrasive hardness has no effect on the erosion wear mechanism of the abrasive but it can affect the roughness of the rock surface. Therefore, under the same incident condition, the abrasive with higher hardness has a greater damage range and erosion depth. This also demonstrates that a hard abrasive has a high erosion efficiency.

#### 4. Conclusions

In this work, rebound particles of the abrasive gas jet are verified to play an important role in the formation of erosion pits. It induces an irregular inverted cone-shaped erosion pit, whereas the bottom of the erosion pit is hemispherical. Besides the rebound particles, the flow field of the gas jet is another primary factor that leads to the formation of an erosion pit. The annular region without an abrasive between the axis and boundary of the jet affects the flow direction of rebound particles, which leads to the formation of an annular platform lying above the hemispherical bottom and under the side of the erosion pit. The erosion wear mechanism of the rock is different in different areas of erosion, because of the involvement of the rebound particles. At the base of the hemispherical bottom, the impact stress wave of the incident abrasive causes rock failure. The rebound abrasive is barely involved in this area. As more and more rebound particles participate in rock erosion, the mechanism of rock erosion is from plastic deformation to fatigue failure. Such as at the

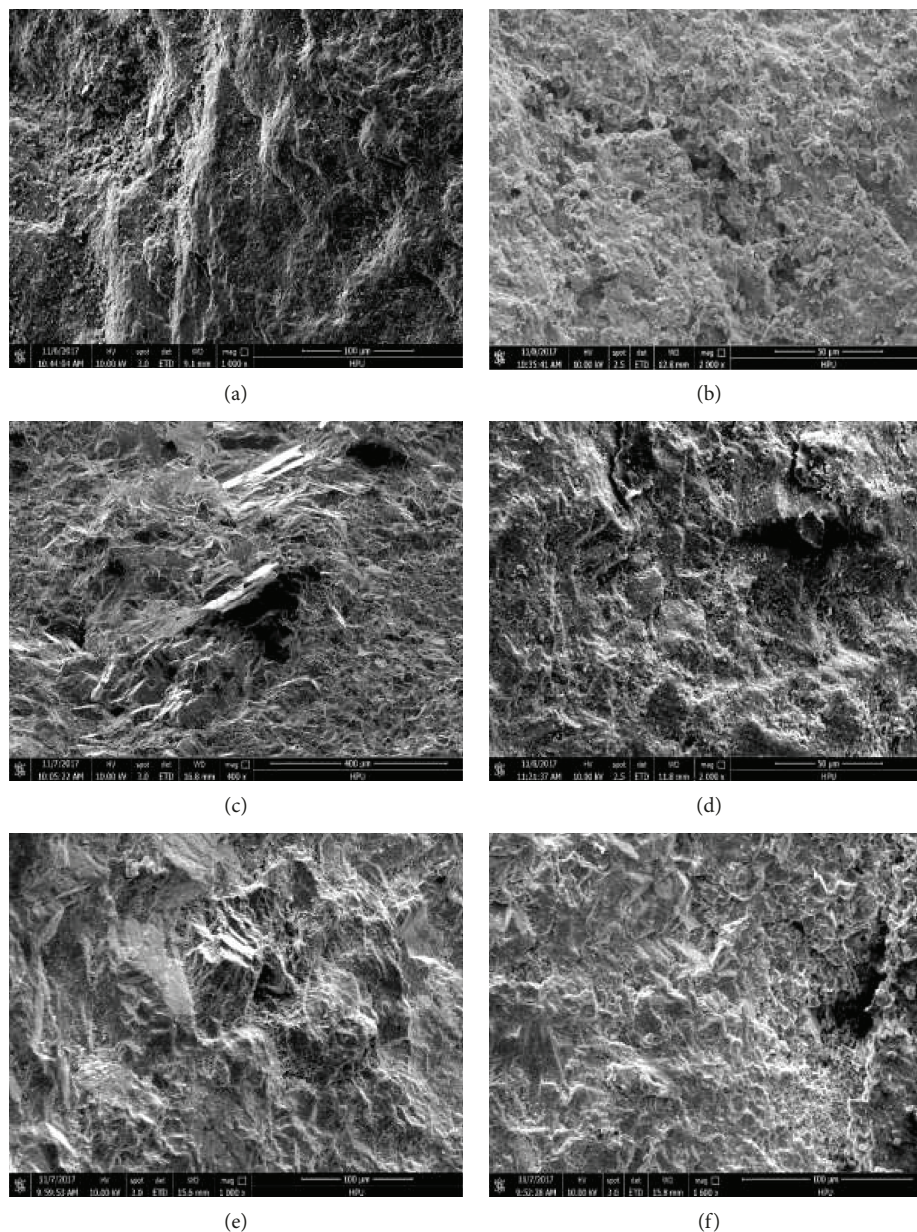


FIGURE 12: SEM images of the side and bottom of the erosion pit.

annular platform, the rock failure is caused by plastic deformation and fatigue failure also occurs; at the side of the erosion pit, the fatigue failure is the main characteristic. Abrasive hardness has no effect on the erosion wear mechanism of the rock. However, hard abrasives are more destructive and can induce a greater erosion depth and rougher surface.

### Data Availability

The data of the paper refers to numerical simulation and experiment. Their calculation method and results are listed in the paper. That is to say, the data used to support the findings of this study are included within the article. We hope that it can give everyone an evidence to judge the conclusion of the paper.

### Conflicts of Interest

The authors declare that they have no conflicts of interest.

### Acknowledgments

This paper was jointly funded by the National Science Foundation of China (51704096, 51604092), the National Key Research and Development Program of China (2017YFC0804207), the Program for Innovative Research Team in University (IRT\_16R22), the Science Research Funds for the Universities of Henan Province (J2018-4), and the Scientific Research Foundation of State Key Laboratory Cultivation Base for Gas Geology and Gas Control (WS2017A02).

## References

- [1] J. M. Fan, C. Y. Wang, and J. Wang, "Modelling the erosion rate in micro abrasive air jet machining of glasses," *Wear*, vol. 266, no. 9-10, pp. 968-974, 2009.
- [2] H. Nouraei, A. Wodoslawsky, M. Papini, and J. K. Spelt, "Characteristics of abrasive slurry jet micro-machining: a comparison with abrasive air jet micro-machining," *Journal of Materials Processing Technology*, vol. 213, no. 10, pp. 1711-1724, 2013.
- [3] J. Wang, A. Moridi, and P. Mathew, "Micro-grooving on quartz crystals by an abrasive air jet," *Proceedings of the Institution of Mechanical Engineers Part C-Journal of Mechanical Engineering Science*, vol. 225, no. 9, pp. 2161-2173, 2011.
- [4] H. Z. Wang, G. S. Li, Z. G. He, Z. H. Shen, M. Wang, and Y. W. Wang, "Mechanism study on rock breaking with supercritical carbon dioxide jet," *Atomization and Sprays*, vol. 27, no. 5, pp. 383-394, 2017.
- [5] H. Z. Wang, G. S. Li, Z. H. Shen et al., "Experiment on rock breaking with supercritical carbon dioxide jet," *Journal of Petroleum Science and Engineering*, vol. 127, pp. 305-310, 2015.
- [6] H. Z. Wang, M. Wang, B. Yang, Q. Lu, Y. Zheng, and H. Q. Zhao, "Numerical study of supercritical CO<sub>2</sub> and proppant transport in different geometrical fractures," *Greenhouse Gases: Science and Technology*, vol. 8, no. 5, pp. 898-910, 2018.
- [7] Y. Liu, B. C. Liang, and X. T. Liu, "Experimental and numerical optimization of coal breakage performance parameters through abrasive gas jet," *International Journal of Heat and Technology*, vol. 35, no. 4, pp. 747-754, 2017.
- [8] Z. Wen, B. Liang, and X. Liu, "Experimental study on influence of abrasive characteristics on coal breaking by abrasive gas jet," *Zhongguo Anquan Shengchan Kexue Jishu*, vol. 103, 2017.
- [9] Y. Liu, J. Wei, and T. Ren, "Analysis of the stress wave effect during rock breakage by pulsating jets," *Rock Mechanics and Rock Engineering*, vol. 49, no. 2, pp. 503-514, 2016.
- [10] Y. Liu, J. Wei, T. Ren, and Z. Lu, "Experimental study of flow field structure of interrupted pulsed water jet and breakage of hard rock," *International Journal of Rock Mechanics and Mining Sciences*, vol. 78, pp. 253-261, 2015.
- [11] Y. Lu, F. Huang, X. Liu, and X. Ao, "On the failure pattern of sandstone impacted by high-velocity water jet," *International Journal of Impact Engineering*, vol. 76, pp. 67-74, 2015.
- [12] M. Mieszala, P. L. Torrubia, D. A. Axinte et al., "Erosion mechanisms during abrasive waterjet machining: model microstructures and single particle experiments," *Journal of Materials Processing Technology*, vol. 247, pp. 92-102, 2017.
- [13] V. Hadavi, C. E. Moreno, and M. Papini, "Numerical and experimental analysis of particle fracture during solid particle erosion, part I: modeling and experimental verification," *Wear*, vol. 356-357, pp. 135-145, 2016.
- [14] V. Hadavi, C. E. Moreno, and M. Papini, "Numerical and experimental analysis of particle fracture during solid particle erosion, part II: effect of incident angle, velocity and abrasive size," *Wear*, vol. 356-357, pp. 146-157, 2016.
- [15] A. Limpichaipanit and R. I. Todd, "The relationship between microstructure, fracture and abrasive wear in Al<sub>2</sub>O<sub>3</sub>/SiC nanocomposites and microcomposites containing 5 and 10% SiC," *Journal of the European Ceramic Society*, vol. 29, no. 13, pp. 2841-2848, 2009.
- [16] A. Momber, "Bruchbilder in Kalknatronglas nach Kontaktbeanspruchung mit hohen Andruckkräften," *Forschung im Ingenieurwesen*, vol. 75, no. 3, pp. 165-182, 2011.
- [17] A. Momber, "Fracture features in soda-lime glass after testing with a spherical indenter," *Journal of Materials Science*, vol. 46, no. 13, pp. 4494-4508, 2011.
- [18] A. W. Momber, "Wear of rocks by water flow," *International Journal of Rock Mechanics and Mining Sciences*, vol. 41, no. 1, pp. 51-68, 2004.
- [19] A. W. Momber, "A probabilistic model for the erosion of cement-based composites due to very high-speed hydro-abrasive flow," *Wear*, vol. 368-369, pp. 39-44, 2016.
- [20] A. W. Momber, "A refined model for solid particle rock erosion," *Rock Mechanics and Rock Engineering*, vol. 49, no. 2, pp. 467-475, 2016.
- [21] R. Brown, S. Kosco, and E. J. Jun, "The effect of particle shape and size on erosion of aluminum alloy 1100 at 90° impact angles," *Wear*, vol. 88, no. 2, pp. 181-193, 1983.
- [22] T. Deng, A. R. Chaudhry, M. Patel, I. Hutchings, and M. S. A. Bradley, "Effect of particle concentration on erosion rate of mild steel bends in a pneumatic conveyor," *Wear*, vol. 258, no. 1-4, pp. 480-487, 2005.
- [23] R. Macchini, M. S. A. Bradley, and T. Deng, "Influence of particle size, density, particle concentration on bend erosive wear in pneumatic conveyors," *Wear*, vol. 303, no. 1-2, pp. 21-29, 2013.
- [24] V. B. Nguyen, Q. B. Nguyen, C. Y. H. Lim, Y. W. Zhang, and B. C. Khoo, "Effect of air-borne particle-particle interaction on materials erosion," *Wear*, vol. 322-323, pp. 17-31, 2015.
- [25] Q. B. Nguyen, V. B. Nguyen, C. Y. H. Lim et al., "Effect of impact angle and testing time on erosion of stainless steel at higher velocities," *Wear*, vol. 321, pp. 87-93, 2014.
- [26] K. Sugiyama, K. Harada, and S. Hattori, "Influence of impact angle of solid particles on erosion by slurry jet," *Wear*, vol. 265, no. 5-6, pp. 713-720, 2008.
- [27] G. P. Tilly, "A two stage mechanism of ductile erosion," *Wear*, vol. 23, no. 1, pp. 87-96, 1973.
- [28] G. Fowler, I. R. Pashby, and P. H. Shipway, "The effect of particle hardness and shape when abrasive water jet milling titanium alloy Ti6Al4V," *Wear*, vol. 266, no. 7-8, pp. 613-620, 2009.
- [29] Z. Mazur, R. Campos-Amezcuca, and A. Campos-Amezcuca, "Shape modification of an axial flow turbine nozzle to reduce erosion," *International Journal of Numerical Methods for Heat & Fluid Flow*, vol. 19, no. 2, pp. 242-258, 2009.
- [30] G. A. Petasyuk, "System and criterial method of the identification and quantitative estimation of the geometrical shape of the abrasive powder grain projection," *Powder Technology*, vol. 264, pp. 78-85, 2014.
- [31] C. G. Telfer, M. M. Stack, and B. D. Jana, "Particle concentration and size effects on the erosion-corrosion of pure metals in aqueous slurries," *Tribology International*, vol. 53, pp. 35-44, 2012.
- [32] J. X. Deng, "Erosion wear of boron carbide ceramic nozzles by abrasive air-jets," *Materials Science and Engineering: A*, vol. 408, no. 1-2, pp. 227-233, 2005.
- [33] J. X. Deng, L. L. Liu, J. H. Liu, X. F. Yang, and M. W. Ding, "Erosion wear behavior and failure mechanisms of ceramic nozzles," *Rare Metal Materials and Engineering*, vol. 34, pp. 223-226, 2005.

- [34] Y. H. Feng, J. X. Deng, and Z. L. Ding, "Erosion wear of ceramic sandblasting nozzles," *Rare Metal Materials and Engineering*, vol. 31, pp. 178–181, 2002.
- [35] I. Konyashin and B. Ries, "Wear damage of cemented carbides with different combinations of WC mean grain size and co content. Part II: laboratory performance tests on rock cutting and drilling," *International Journal of Refractory Metals & Hard Materials*, vol. 45, pp. 230–237, 2014.
- [36] C. Trevisiol, A. Jourani, and S. Bouvier, "Effect of hardness, microstructure, normal load and abrasive size on friction and on wear behaviour of 35NCD16 steel," *Wear*, vol. 388–389, pp. 101–111, 2017.
- [37] Y. Liu, J. Zhang, T. Zhang, and H. D. Zhang, "Optimal nozzle structure for an abrasive gas jet for rock breakage," *Geofluids*, vol. 2018, Article ID 9457178, 14 pages, 2018.
- [38] Z. H. Wen, Y. Liu, X. T. Liu, and B. C. Liang, "Experimental research into the effects of abrasive characteristics on abrasive gas jet coal-breaking performance," *International Journal of Heat and Technology*, vol. 35, no. 1, pp. 32–36, 2017.
- [39] N. Koutsourakis, J. G. Bartzis, and N. C. Markatos, "Evaluation of Reynolds stress,  $k-\epsilon$  and RNG  $k-\epsilon$  turbulence models in street canyon flows using various experimental datasets," *Environmental Fluid Mechanics*, vol. 12, no. 4, pp. 379–403, 2012.
- [40] Z. Amiri and S. Movahedirad, "Bubble-induced particle mixing in a 2-D gas-solid fluidized bed with different bed aspect ratios: a CFD-DPM study," *Powder Technology*, vol. 320, pp. 637–645, 2017.
- [41] H. Ling, F. Li, L. Zhang, and A. Conejo, "Investigation on the effect of nozzle number on the recirculation rate and mixing time in the RH process using VOF + DPM model," *Metallurgical and Materials Transactions B*, vol. 47, no. 3, pp. 1950–1961, 2016.
- [42] H. Wang, W. Nie, W. Cheng, Q. Liu, and H. Jin, "Effects of air volume ratio parameters on air curtain dust suppression in a rock tunnel's fully-mechanized working face," *Advanced Powder Technology*, vol. 29, no. 2, pp. 230–244, 2018.
- [43] Y. Liu, T. Zhang, and X. T. Liu, "Analysis of the stress wave effect during coal breakage by a high-pressure abrasive air jet," *Advances in Mechanical Engineering*, vol. 10, no. 6, 2018.
- [44] Y. Z. Xue, H. Si, and Q. T. Hu, "The propagation of stress waves in rock impacted by a pulsed water jet," *Powder Technology*, vol. 320, pp. 179–190, 2017.
- [45] I. Belyatinskaya, V. Fel'Dman, V. Milyavsky, T. Borodina, and A. Belyakov, "Transformations of rock-forming minerals under stepwise shockwave compression of quartz-feldspar-biotite-garnet schist from the Southern Urals," *Moscow University Geology Bulletin*, vol. 67, no. 1, pp. 30–42, 2012.
- [46] M. Petrica, E. Badisch, and T. Peinsitt, "Abrasive wear mechanisms and their relation to rock properties," *Wear*, vol. 308, no. 1–2, pp. 86–94, 2013.
- [47] Y. Ju, H. J. Wang, Y. M. Yang, Q. A. Hu, and R. D. Peng, "Numerical simulation of mechanisms of deformation, failure and energy dissipation in porous rock media subjected to wave stresses," *Science China-Technological Sciences*, vol. 53, no. 4, pp. 1098–1113, 2010.
- [48] M. S. Suh, T. Hinoki, and A. Kohyama, "Erosive wear mechanism of new SiC/SiC composites by solid particles," *Tribology Letters*, vol. 41, no. 3, pp. 503–513, 2011.
- [49] P. N. W. Verhoef, "Sandblast testing of rock," *International Journal of Rock Mechanics and Mining Sciences & Geomechanics Abstracts*, vol. 24, no. 3, pp. 185–192, 1987.



**Hindawi**

Submit your manuscripts at  
[www.hindawi.com](http://www.hindawi.com)

